Continuously observing a dynamically decoupled spin-1 quantum gas

R. P. Anderson, M. J. Kewming, and L. D. Turner
School of Physics and Astronomy, Monash University, Melbourne, Victoria 3800, Australia

(Received 27 June 2017; published 16 January 2018)

We continuously observe dynamical decoupling in a spin-1 quantum gas using a weak optical measurement of spin precession. Continuous dynamical decoupling modifies the character and energy spectrum of spin states to render them insensitive to parasitic fluctuations. Continuous observation measures this new spectrum in a single preparation of the quantum gas. The measured time series contains seven tones, which spectrogram analysis parses as splittings, coherences, and coupling strengths between the decoupled states in real time. With this we locate a regime where a transition between two states is decoupled from magnetic-field instabilities up to fourth order, complementary to a parallel work at higher fields [D. Trypogeorgos *et al.*, preceding paper, Phys. Rev. A **97**, 013407 (2018)]. The decoupled microscale quantum gas offers magnetic sensitivity in a tunable band, persistent over many milliseconds: the length scales, frequencies, and durations relevant to many applications, including sensing biomagnetic phenomena such as neural spike trains.

DOI: 10.1103/PhysRevA.97.013408

I. INTRODUCTION

From Hahn echoes to dynamical decoupling, pulse sequences have been used to protect spin superpositions from inhomogeneities and parasitic fluctuations, prolonging quantum coherence and circumventing deleterious energy shifts [1–3]. A complementary strategy is continuous dynamical decoupling: replacing the pulse sequence with an uninterrupted coupling of bare spin states yielding dressed spin eigenstates with new quantization direction, spectrum, and coupling. The new spectrum protects against low-frequency fluctuations, while the new couplings admit band-tunable sensing [4]. Continuous dynamical decoupling has been applied to nitrogen-vacancy centers [5–8], atomic microwave clocks [9,10], and superconducting qubits and creates protected qubit [11,12] and decoherence-free [13] subspaces. Marrying continuous dynamical decoupling with weak continuous measurement could give rise to new forms of quantum sensing exploiting synchronous detection and feedback [14].

Here we demonstrate how a weak continuous measurement of spin precession can probe the spectrum of a continuously decoupled spin-1 quantum gas in a single experimental preparation (shot). Time-resolved Fourier spectroscopy of this measurement reveals not only all dressed-state splittings and their relative immunity to noise, but also dressed-state coherences and coupling strengths. The eigenspectrum of the multilevel dressed system brings into view a higher-order decoupling than exists in dynamically decoupled two-level systems. One transition may be only quartically sensitive to noise, tolerating much larger fluctuations than with conventional quadratic decoupling. Further, a new transition arises between states that are otherwise uncoupled, completing a cyclic coupling of all dressed states. This low-frequency magnetic stability combined with continuous detection is immediately applicable to band-tunable magnetometry [5,6,15] and experiments preparing delicate spin-entangled many-body states [16], whereas the unconventional cyclic coupling could be applied to emulation of frustrated quantum spin chains [17].

II. SPIN-1 CONTINUOUS DYNAMICAL DECOUPLING

Atomic Zeeman states $|m_z = -1,0,1\rangle$ in a magnetic field $B_z\mathbf{e}_z$ are decoupled from fluctuations in B_z by applying a perpendicular radio-frequency (rf) field $B_{\rm rf}\mathbf{e}_x \cos\omega_{\rm rf}t$, tuned near the Larmor frequency $\omega_L \equiv (E_{m_z=-1} - E_{m_z=+1})/2\hbar$. At low fields, the degeneracy of the composite spin-1/2 systems [18] renders the spin-1 behavior identical to continuous dynamical decoupling in spin-1/2 systems. The spin is quantized along $\Omega = \Omega\,\mathbf{e}_x + \Delta\,\mathbf{e}_z$ in a frame rotating at $\omega_{\rm rf}$; the eigenvalues of $\mathcal{H}_{\rm rwa} = \Delta\hat{F}_z + \Omega\hat{F}_x$ are $m_x\hbar\sqrt{\Omega^2+\Delta^2}$, where $\Delta = \omega_{\rm rf} - \omega_L$ is the detuning, Ω is the Rabi frequency, and $|m_x = -1,0,1\rangle$ is the corresponding eigenstate at resonance. Dressing induces an avoided crossing in the spectrum; whereas the bare-state energies are linearly sensitive to magnetic-field variations δB_z ($\omega_L \approx \gamma B_z$, where γ is the gyromagnetic ratio), the dressed energies are only quadratically sensitive near resonance ($\Delta = 0$).

The spin character and symmetries are otherwise unchanged: Transverse magnetic fields oscillating near the splitting frequencies drive transitions between eigenstates. In the dressed system this means that relatively low-frequency (ac) fields oscillating near the Rabi frequency, along z, drive transitions $|m_x = -1\rangle \leftrightarrow |m_x = 0\rangle$ and $|m_x = 0\rangle \leftrightarrow |m_x = +1\rangle$. This is the basis for ac magnetometry [5] and for concatenated dynamical decoupling which protects against fluctuations in Ω [7,19]. Insensitivity to wider bandwidth and larger amplitude δB_z can be achieved by increasing Ω, opening a broader gap in the dressed spectrum, but doing so changes the detection band of ac magnetometry [6] or pulsed dynamical decoupling [20]. Henceforth we presume that Ω is fixed by the application.

Any $\hat{F}_z^2$ interaction, from nonlinear Zeeman [21], microwave ac Stark [22], or tensor light [23] shifts, raises the degeneracy of the $|m_z = -1\rangle \leftrightarrow |m_z = 0\rangle$ and $|m_z = 0\rangle \leftrightarrow |m_z = +1\rangle$ transitions. Now $\mathcal{H}_{\rm RWA} = \Delta\hat{F}_z + \Omega\hat{F}_x + q\hat{F}_z^2/\hbar$, where the quadratic Zeeman shift $q \equiv (E_{m_z=+1} + E_{m_z=-1} - 2E_{m_z=0})_{\Omega=0}/2\hbar$. This yields dressed eigenstates $\{|1\rangle,|2\rangle,|3\rangle\}$ with eigenspectrum $\omega_i(\Delta) = E_{|i\rangle}/\hbar$ shown in Fig. 1 (left).

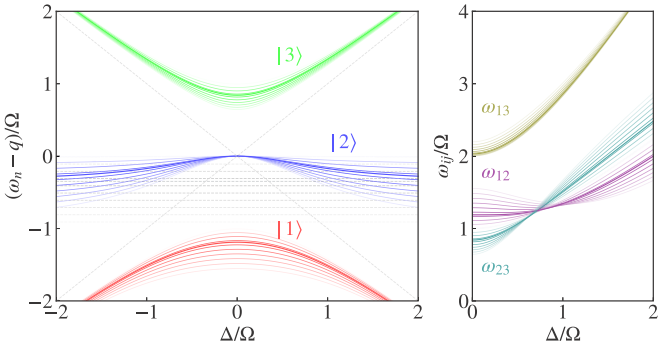

FIG. 1. Energy spectrum and splittings of a radio-frequency coupled spin-1 for several $q_R = q/\Omega$ between 0 and 1. The boldest curves have $q_R = q_{R,\mathrm{magic}}$. Shown on the left are energies ω_n of dressed states $|n\rangle = |1\rangle$ (red), $|2\rangle$ (blue), and $|3\rangle$ (green) normalized to the Rabi frequency. Dashed lines indicate the energies of uncoupled states ($\Omega = 0$) in a frame rotating at ω_{rf}. Shown on the right are splittings $\omega_{ij} = \omega_j - \omega_i$ of dressed states $|i\rangle$ and $|j\rangle$ as a function of detuning. When $q_R = q_{R,\mathrm{magic}}$ (bold curves), ω_1 and ω_2 share the same curvature and their difference ω_{12} is minimally sensitive to detuning and thus magnetic-field variations.

Moreover, the couplings between these dressed states when $q \neq 0$ are markedly different: $\langle 1|\hat{F}_{y,z}|2\rangle$ and $\langle 2|\hat{F}_{y,z}|3\rangle$ remain nonvanishing but $\langle 1|\hat{F}_x|3\rangle$ becomes nonzero. The transitions are thus cyclic ($|1\rangle \leftrightarrow |2\rangle \leftrightarrow |3\rangle \leftrightarrow |1\rangle$) and nondegenerate, characterized by a dressed Larmor frequency $\omega_D \equiv (\omega_3 - \omega_1)/2$ and dressed quadratic shift $q_D \equiv (\omega_3 + \omega_1 - 2\omega_2)/2$, giving splittings $\omega_{23} = \omega_D - q_D$, $\omega_{12} = \omega_D + q_D$, and $\omega_{13} = 2\omega_D$. On resonance, $\omega_D = \sqrt{\Omega^2 + q_D^2}$ and $q_D = -q/2$.

A figure of merit for decoupling is the curvature of the transition frequency at resonance. Figure 1 shows that in the spin-1 system with quadratic shift, two states are convex, suggesting that a regime may exist in which the curvature of their transition frequency vanishes [24]. Indeed, we find an analytic value of the normalized quadratic shift $q_R = q/\Omega$ where the curvatures of ω_1 and ω_2 are equal,[1]

$$q_{R,\mathrm{magic}} = \sqrt{(3\sqrt{2} - 4)/2} \approx 0.348, \tag{1}$$

resulting in the vanishing quadratic dependence of the transition frequency ω_{12} on Δ. The leading-order sensitivity of these states to field variations δB_z at $q_{R,\mathrm{magic}}$ is quartic,[2] giving the subspace comprised of $|1\rangle$,$|2\rangle$ a higher-order decoupling than can be achieved with a two-level system; we term these hyperdecoupled states.

[1]The curvature of the dressed-state energies is evaluated using perturbation theory. In particular, the dimensionless curvature of ω_{12} is $\partial^2(\omega_{12}/\Omega)/\partial(\Delta/\Omega)^2 = \Omega\partial^2\omega_{12}/\partial\Delta^2 = -(3q_R\sqrt{4+q_R^2} - q_R^2 - 2)/\sqrt{4+q_R^2}$. For $q_R = 0$, we recover the spin-1/2 result $\Omega\partial^2\omega_{12}/\partial\Delta^2 = 1$.

[2]We take $\Delta = -\gamma\delta B_z$ for $|\Delta| \leqslant 2\Omega$ ($|\delta B_z| \leqslant B_{\mathrm{rf}}/2$) and $|\partial q/\partial\Delta| \approx |\gamma^{-1}\partial q/\partial B_z| = |2B_z q_Z/\gamma| \ll 1$, valid to 10^{-3} for the field strengths $B_z \lesssim 5$ G used here, resulting in vanishing third-order derivatives of ω_i with respect to detuning. In general, the variation of q with Δ (or δB_z) can be accounted for using the Breit-Rabi equation, leading to a residual linear and cubic variation of ω_{12} with δB_z [25].

III. CONTINUOUSLY OBSERVING A HYPERDECOUPLED QUANTUM GAS

We explore this high-order decoupling with a continuous measurement of the dressed spectrum of a spin-1 nondegenerate quantum gas. Using a single realization of the quantum gas, we make many successive weak measurements, revealing all three splittings ω_{ij} simultaneously. Our spinor quantum gas apparatus [26] and Faraday atom-light interface [27] are described elsewhere. We prepare an ultracold gas ($\sim$1 μK) of approximately 10^6 ^{87}Rb atoms in a crossed-beam optical dipole trap. A radio-frequency field of amplitude $\Omega/2\pi \leqslant 100$ kHz couples the three Zeeman states $|m_z = -1,0,+1\rangle$ of the lowest hyperfine ground state. To perform a weak measurement of the evolving spin, we focus onto the atoms a linearly polarized far-off-resonance probe beam ($\lambda = 781.15$ nm, detuned -0.45 THz) propagating along x. The spin component parallel to the wave vector of the probe rotates its polarization via the paramagnetic Faraday effect; shot-noise-limited polarimetry measures $\langle\hat{F}_x\rangle$ as a modulated tone near ω_L.

To probe the dressed-state spectrum and coherences, we prepare a superposition of dressed states by suddenly turning on Rabi coupling Ω, projecting the polarized collective spin $|m_z = -1\rangle$ onto $|\psi(t=0)\rangle = \sum_i c_i|i\rangle$. The total magnetic field in the laboratory frame is $\mathbf{B}(t \geqslant 0) = -B_{\mathrm{rf}}\cos(\omega_{\mathrm{rf}}t)\mathbf{e}_x + B_z(t)\mathbf{e}_z$, where $B_z(t)$ varies slowly compared to Ω. The resulting Faraday signal is analyzed in the time-frequency domain using the short-time Fourier transform (STFT), revealing the rich frequency and amplitude modulation arising from the dressed-state energies, coherences, and coupling strengths. Weak measurement allows this Fourier transform spectroscopy to be performed many times in one shot (cf. [28]).

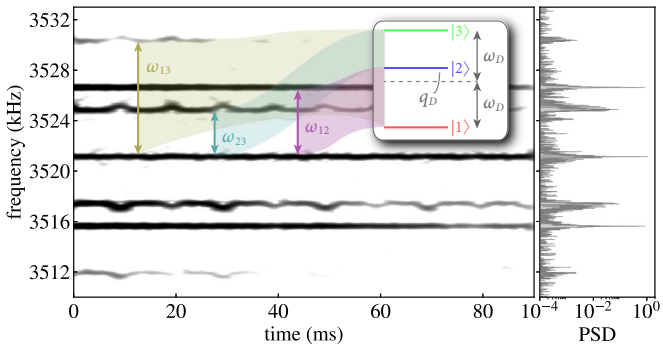

FIG. 2. Continuous measurement of the dressed energy spectrum for $q_R = 0.402(3)$, $f_{\mathrm{rf}} = 3.521$ MHz, and $B_0 = 5.013$ G: spectrogram (left) and power spectral density (PSD) (normalized) (right) of the 90-ms-long signal. The inset shows the dressed-state energy diagram; the mean and difference of transition frequencies ω_{12} and ω_{23} are the dressed Larmor frequency ω_D and quadratic shift q_D, respectively. The sidebands about the carrier at f_{rf} are associated with the ω_{13} (gold), ω_{23} (turquoise), and ω_{12} (lavender) transitions. Magnetic-field fluctuations are manifest as asymmetric frequency modulation of the ω_{13} and ω_{23} sidebands, while the ω_{12} transition remains relatively unaffected. The corresponding peaks in the PSD have linewidths 102, 97, and 24 Hz (near transform limited), respectively. The ω_{23} peaks are significantly skewed (the mean magnitude of the Pearson skew coefficient is 0.88), while the ω_{12} peaks are unskewed (Pearson skew coefficient 0.08).

TABLE I. Upper sidebands of the Faraday rotation signal proportional to $\langle \hat{F}_x \rangle$ of an arbitrary dressed-state superposition. Each sideband is identified with a dressed-state transition $|i\rangle \leftrightarrow |j\rangle$. Sideband amplitudes are for resonant coupling, and for the initial state $|\psi(t=0)\rangle = |m_z = -1\rangle$ these are concisely expressed in terms of the dressed Larmor frequency ω_D and quadratic shift q_D. Each upper sideband has a lower sideband of the same amplitude, relative frequency, and opposite phase.

Transition	Frequency	$\omega_{ij} - \omega_{\rm rf}$	Amplitude ($\Delta = 0$)	Amplitude ($\Delta = 0, \lvert m_z = -1\rangle$)
(carrier)	$\omega_{\rm rf}$	0	$(\langle 3\lvert \hat{F}_x \rvert 3\rangle - \langle 1\lvert \hat{F}_x \rvert 1\rangle)(\rho_{33} - \rho_{11})$	$\hbar q_D \Omega / 2\omega_D^2$
$\lvert 1\rangle \leftrightarrow \lvert 2\rangle$	$\omega_{\rm rf} + \omega_{12}$	$\omega_D + q_D$	$-2i\langle 1\lvert \hat{F}_y \rvert 2\rangle \mathrm{Re}\,\rho_{12} = -2\langle 2\lvert \hat{F}_z \rvert 3\rangle \mathrm{Re}\,\rho_{12}$	$\hbar\Omega/4\omega_D$
$\lvert 2\rangle \leftrightarrow \lvert 3\rangle$	$\omega_{\rm rf} + \omega_{23}$	$\omega_D - q_D$	$2i\langle 2\lvert \hat{F}_y \rvert 3\rangle \mathrm{Re}\,\rho_{23} = 2\langle 1\lvert \hat{F}_z \rvert 2\rangle \mathrm{Re}\,\rho_{23}$	$\hbar\Omega/4\omega_D$
$\lvert 1\rangle \leftrightarrow \lvert 3\rangle$	$\omega_{\rm rf} + \omega_{13}$	$2\omega_D$	$2\langle 1\lvert \hat{F}_x \rvert 3\rangle \mathrm{Re}\,\rho_{13}$	$\hbar q_D \Omega / 4\omega_D^2$

With no deliberate variation of the Rabi frequency or detuning, we observe the STFT amplitude (spectrogram) shown in Fig. 2. Strong amplitude modulation of the Faraday signal is apparent as three pairs of sidebands, each equidistant from the carrier frequency $f_{\rm rf} = \omega_{\rm rf}/2\pi$. Each pair of sidebands corresponds to a dressed-state transition $|i\rangle \leftrightarrow |j\rangle$, with sideband frequencies $f_{\rm rf} \pm f_{ij}$, where $f_{ij} = \omega_{ij}/2\pi$. Thus the spectrogram is a calibration-free, real-time measurement of the dressed-state spectrum. Considering the upper sidebands, the two closest to the carrier are from adjacent state transitions ω_{12} and ω_{23} with similar amplitudes and at frequencies $\omega_D \pm q_D$ above the carrier. The third, weaker sideband $2\omega_D$ above the carrier signifies the cyclic $|1\rangle \leftrightarrow |3\rangle$ transition, appearing when $q \neq 0$. The apparatus is not shielded from magnetic noise and the power line causes a $\delta B_z = \delta B_{\rm line}(t)$ at 50 Hz and its odd harmonics. Each dressed transition is affected by the magnetic fluctuations differently: The sidebands corresponding to the ω_{13} and ω_{23} transitions exhibit asymmetric frequency modulation, whereas the optimally decoupled ω_{12} transition remains unperturbed within the frequency resolution of this spectrogram.

The amplitude of each sideband is proportional to the corresponding dressed-state coherence $\rho_{ij} = c_i^* c_j$ and the nonvanishing dressed-state coupling(s) $\langle i|\hat{F}_{x,y,z}|j\rangle$, as summarized for near-resonant coupling ($|\Delta| \ll \Omega$) in Table I. If the projection onto the dressed basis (and hence ρ_{ij}) is known, our measurement constitutes a single-shot estimation of the coupling strengths. Alternatively, if the couplings are separately characterized [25], this amounts to continuous measurement of the dressed density matrix, effecting quantum state estimation of the dressed system.

Different platforms use different metrics for the fidelity of dynamical decoupling and in addition to linewidth narrowing include prolonged coherence. We observe a threefold increase in the lifetime of the spectral components corresponding to the ω_{12} and ω_{23} transitions as compared with the undressed system [Fig. 3(a), $1/e$ decay time 23.8(2) ms]. Dressed-state coherences are expected to last longer, but were limited here by the ∼100-ms probe-induced photon scattering time. A less perturbative probe [27] should reveal even longer dressed coherence times at the expense of signal-to-noise ratio.

To better expose the enhanced insensitivity of the hyperdecoupled states in the vicinity of $q_{R,\rm magic}$, we sweep the the magnetic field over a wider range than is furnished by the power line noise. The longitudinal field $B_z(t) = B_0 + \alpha t + B_{\rm line}(t)$, where $\alpha = 128$ mG/s is the linear sweep rate; the resulting detuning sweeps across 2Ω (the domain of Fig. 1) during the single-shot measurement. We interleave each rf-dressed shot with a magnetometry shot calibrating $B_z(t)$: An rf $\pi/2$ pulse initiates Larmor precession of the undressed collective spin and the Faraday signal is composed of two tones at $\omega_\pm = \omega_L \pm q$, the Zeeman splittings (Fig. 3, top). For spectrogram windows $\tau_f > 2\pi/q$ the frequencies $\omega_\pm$ are resolved, yielding the instantaneous $\omega_L(t)$ and $q(t)$. We then use $\omega_L(t)$ to find $\delta B_z(t)$ [and $\Delta(t)$] by inverting the Breit-Rabi equation [21].

We measure the dressed spectrum for resonant magnetic fields B_0 ranging from 3.549 to 5.568 G, with a mean Rabi frequency of $\Omega/2\pi = 4.505(3)$ kHz. At each field B_0 we ensure that the Rabi frequency is fixed by measuring the voltage drop across the coil at $f_{\rm rf}$ with an rf lock-in amplifier. The Rabi frequency is ultimately measured using the atoms by analyzing the dressed energy spectrum near resonance ($|\Delta|/2\pi \leqslant 100$ Hz) where $\Omega = \sqrt{\omega_{12}\omega_{23}}$. The measured Rabi frequencies have a standard deviation $\sigma(\Omega)/2\pi = 9.4$ Hz, validating the method.

Figure 3 shows the dressed spectrum measured as δB_z varies across a range $\sim B_{\rm rf}$ during a single shot. The instantaneous dressed-state splittings for all three transitions are predicted with no free parameters and plotted atop the spectrogram data, showing excellent agreement with the measured sidebands. Line noise renders $\delta B_z(t)$ nonmonotonic. By tracking the instantaneous peaks in the calibration and dressed spectrograms we plot $(\delta B_z(t), f_{ij}(t))$ parametrically, eliminating the line noise systematic. The sensitivity of the $|1\rangle \leftrightarrow |2\rangle$ and $|2\rangle \leftrightarrow |3\rangle$ transitions to magnetic-field variations is shown in Fig. 3(c). The hyperdecoupled transition is least sensitive; f_{12} varies by 39 Hz for δB_z up to $\Omega/2\gamma = 3.2$ mG [Fig. 3(c), inset]. Normalizing the variation to the Rabi frequency makes possible a comparison of decoupling across platforms and ac magnetometry bandwidths. The normalized variation $\delta\omega_{12}/\Omega = 8.6 \times 10^{-3}$ over $0 < |\Delta| < \Omega/2$. Conventional decoupling ($q_R = 0$) has variation $(\sqrt{5} - 2)/2 \approx 0.118$ across this range, while the undressed Zeeman transitions in the low-field limit have a normalized variation of 0.5.

To optimally suppress the sensitivity of the hyperdecoupled states to small field variations, we experimentally determine the curvature of ω_{12} for q_R between 0.2 and 0.5, independent of the predicted spectrum of $\mathcal{H}_{\rm RWA}$. For each q_R, we fit a polynomial to $(\delta B_z, f_{12})$ data extracting $\partial^2 f_{12}/\partial B_z^2$ (Fig. 4). A linear fit of the measured curvature versus q_R infers $q_{R,\rm magic}$ (expt) = 0.350(6). The predictive power of the measured dressed spectrum and this model-independent analysis is affirmed

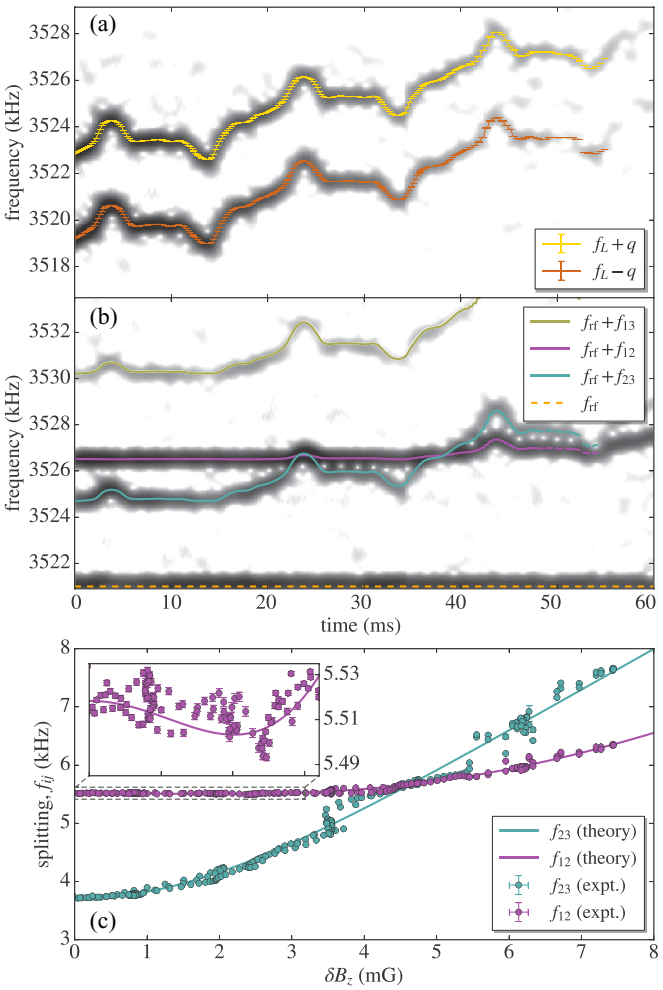

FIG. 3. Real-time observation of continuous dynamical decoupling for $q_R = 0.402(3)$. (a) and (b) Spectrograms of a continuous weak measurement of $\langle \hat{F}_x \rangle$. (a) Magnetometry of the bare Zeeman states is used to calibrate $B_z(t) = B_0 + \delta B_z(t)$ during the measurement interval, in which the detuning varies over a range $\sim 2\Omega$. We numerically track the Zeeman splittings (gold and orange lines) to determine the instantaneous Larmor frequency $\omega_L(t)$ and quadratic shift $q(t)$. (b) The field is swept over the same range but the rf dressing is applied [$\Omega/2\pi = 4.520(2)$ kHz]. Three sidebands above (shown) and below the carrier at $f_{rf} = 3.521$ MHz (dashed orange line) reveal the dressed-state splittings $f_{ij} = \omega_{ij}/2\pi$. (c) Parametric plot of $f_{12}(t)$ and $f_{23}(t)$ versus $\delta B_z(t)$ by combining the analysis of (a) and (b). Solid curves in (b) and (c) are from an eigenspectrum calculation, provided only f_{rf}, $B_z(t)$, and Ω. The inset in (c) shows the variation of the hyperdecoupled transition f_{12} for $0 \leqslant \delta B_z \leqslant \Omega/2\gamma = 3.2$ mG.

by the agreement with the theoretical curvature (red curve, Fig. 4) and $q_{R,\mathrm{magic}}$ in Eq. (1). In dimensionless units with the splitting and detuning normalized to the Rabi frequency, the lowest curvature we measure is $(\Omega\, \partial^2\omega_{12}/\partial\Delta^2)_{\mathrm{min}} = 0.013,75$ times lower than the curvature of this transition for quadratic decoupling ($q_R = 0$).

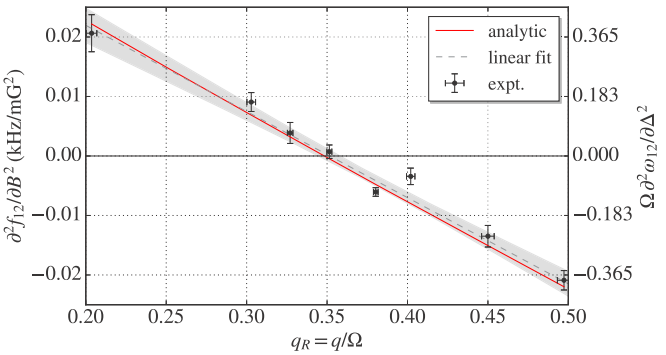

FIG. 4. Curvature of the hyperdecoupled $|1\rangle \leftrightarrow |2\rangle$ transition for normalized quadratic shifts q_R from 0.2 to 0.5. Measured curvature (black points) is determined from polynomial fits to the $(\delta B_z, f_{12})$ data, e.g., Fig. 3(c). Vertical and horizontal error bars correspond to the standard error of the regression and uncertainty in q_R, respectively. A linear fit (black dashed line) with a 1σ confidence band (gray shaded region) is shown; the intercept gives $q_{R,\mathrm{magic}}(\mathrm{expt}) = 0.350(6)$. The analytic expression for the curvature (red) (see footnote 1) is consistent. The left axis is the curvature $\partial^2 f_{12}/\partial B_z^2$ in kHz/G^2. The right axis is $\Omega\,\partial^2\omega_{12}/\partial\Delta^2$, i.e., normalized to the curvature of quadratic decoupling ($q_R = 0$).

This intrashot revelation of the time and frequency domain renders the measurement of these spectra orders of magnitude more efficient. For example, with single-shot (Stern-Gerlach imaging) measurement, the single spectrum shown in Fig. 3 would take order 3 h of data acquisition. We acquired this spectrum in a single 20-s shot; all data for Fig. 4 were acquired in 5 min.

IV. CONCLUSION

In summary, we demonstrate continuous measurement of continuous dynamical decoupling in a spin-1 quantum gas. Continuous weak measurement via the Faraday effect yields information about the rf-dressed superposition, the dressed-state couplings, and energies, simultaneously, making possible full characterization over detunings in one experimental shot. We posit that viewed as an ac magnetometer, this information not only will measure fields oscillating at the dynamically tunable Rabi frequency, but self-certifies both band center and residual detuning error, in real time, while remaining fourth-order decoupled. More broadly, the cyclic coupling we observe may emulate quantum spin ladders with frustrated interactions [17]. Our measurement is readily extended into the backaction regime, where measurement of bare precessing spins induces simultaneous two-axis squeezing [29]. Strong measurement of dressed precessing spins adds the third axis and may expose non-Gaussian quantum noise geometries.

ACKNOWLEDGMENTS

We thank A. A. Wood, I. B. Spielman, N. Lundblad, and F. A. Pollock for enlightening discussions. This work was supported by ARC Grant No. LP130100857 and a Monash University IDR seed grant.

[1] M. J. Biercuk, H. Uys, A. P. VanDevender, N. Shiga, W. M. Itano, and J. J. Bollinger, Nature (London) **458**, 996 (2009).

[2] G. de Lange, Z. H. Wang, D. Ristè, V. V. Dobrovitski, and R. Hanson, Science **330**, 60 (2010).

[3] H. Bluhm, S. Foletti, I. Neder, M. Rudner, D. Mahalu, V. Umansky, and A. Yacoby, Nat. Phys. **7**, 109 (2011).
[4] F. F. Fanchini, J. E. M. Hornos, and R. d. J. Napolitano, Phys. Rev. A **75**, 022329 (2007).
[5] M. Hirose, C. D. Aiello, and P. Cappellaro, Phys. Rev. A **86**, 062320 (2012).
[6] M. Loretz, T. Rosskopf, and C. L. Degen, Phys. Rev. Lett. **110**, 017602 (2013).
[7] J.-M. Cai, B. Naydenov, R. Pfeiffer, L. P. McGuinness, K. D. Jahnke, F. Jelezko, M. B. Plenio, and A. Retzker, New J. Phys. **14**, 113023 (2012); J. Cai, F. Jelezko, N. Katz, A. Retzker, and M. B. Plenio, *ibid.* **14**, 093030 (2012).
[8] D. A. Golter, T. K. Baldwin, and H. Wang, Phys. Rev. Lett. **113**, 237601 (2014).
[9] G. A. Kazakov and T. Schumm, Phys. Rev. A **91**, 023404 (2015).
[10] L. Sárkány, P. Weiss, H. Hattermann, and J. Fortágh, Phys. Rev. A **90**, 053416 (2014).
[11] N. Aharon, M. Drewsen, and A. Retzker, Phys. Rev. Lett. **111**, 230507 (2013).
[12] I. Baumgart, J.-M. Cai, A. Retzker, M. B. Plenio, and C. Wunderlich, Phys. Rev. Lett. **116**, 240801 (2016).
[13] P. Facchi and S. Pascazio, Phys. Rev. Lett. **89**, 080401 (2002); P. Facchi, D. A. Lidar, and S. Pascazio, Phys. Rev. A **69**, 032314 (2004).
[14] R. Vijay, C. Macklin, D. H. Slichter, S. J. Weber, K. W. Murch, R. Naik, A. N. Korotkov, and I. Siddiqi, Nature (London) **490**, 77 (2012).
[15] C. F. Ockeloen, R. Schmied, M. F. Riedel, and P. Treutlein, Phys. Rev. Lett. **111**, 143001 (2013); A. Horsley and P. Treutlein, Appl. Phys. Lett. **108**, 211102 (2016).
[16] D. M. Stamper-Kurn and M. Ueda, Rev. Mod. Phys. **85**, 1191 (2013).
[17] H.-J. Mikeska and A. K. Kolezhuk, in *Quantum Magnetism*, edited by U. Schollwöck, J. Richter, D. J. J. Farnell, and R. F. Bishop, Lecture Notes in Physics Vol. 645 (Springer, Berlin, 2004), pp. 1–83.
[18] E. Majorana, Nuovo Cimento **9**, 43 (1932).
[19] N. Timoney, I. Baumgart, M. Johanning, A. F. Varón, M. B. Plenio, A. Retzker, and C. Wunderlich, Nature (London) **476**, 185 (2011).
[20] J. M. Boss, K. S. Cujia, J. Zopes, and C. L. Degen, Science **356**, 837 (2017); S. Schmitt, T. Gefen, F. M. Stürner, T. Unden, G. Wolff, C. Müller, J. Scheuer, B. Naydenov, M. Markham, S. Pezzagna, J. Meijer, I. Schwarz, M. Plenio, A. Retzker, L. P. McGuinness, and F. Jelezko, *ibid.* **356**, 832 (2017).
[21] N. Ramsey, *Molecular Beams* (Clarendon, Oxford, 1956).
[22] F. Gerbier, A. Widera, S. Fölling, O. Mandel, and I. Bloch, Phys. Rev. A **73**, 041602 (2006).
[23] G. A. Smith, S. Chaudhury, A. Silberfarb, I. H. Deutsch, and P. S. Jessen, Phys. Rev. Lett. **93**, 163602 (2004).
[24] P. Rabl, P. Cappellaro, M. V. G. Dutt, L. Jiang, J. R. Maze, and M. D. Lukin, Phys. Rev. B **79**, 041302(R) (2009); X. Xu, Z. Wang, C. Duan, P. Huang, P. Wang, Y. Wang, N. Xu, X. Kong, F. Shi, X. Rong, and J. Du, Phys. Rev. Lett. **109**, 070502 (2012).
[25] D. Trypogeorgos, A. Valdés-Curiel, N. Lundblad, and I. B. Spielman, preceding paper, Phys. Rev. A **97**, 013407 (2018).
[26] A. A. Wood, L. M. Bennie, A. Duong, M. Jasperse, L. D. Turner, and R. P. Anderson, Phys. Rev. A **92**, 053604 (2015).
[27] M. Jasperse, M. J. Kewming, S. N. Fischer, P. Pakkiam, R. P. Anderson, and L. D. Turner, Phys. Rev. A **96**, 063402 (2017).
[28] A. Valdés-Curiel, D. Trypogeorgos, E. E. Marshall, and I. B. Spielman, New J. Phys. **19**, 033025 (2017).
[29] G. Colangelo, F. M. Ciurana, L. C. Bianchet, R. J. Sewell, and M. W. Mitchell, Nature (London) **543**, 525 (2017).